Supporting Information

Enhancement of single photon emission from nitrogen-vacancy centers with TiN/(Al,Sc)N hyperbolic metamaterial

M. Y. Shalaginov[1,2,*], V. V. Vorobyov[3,4,*], J. Liu[5], M. Ferrera[1,2,7], A. V. Akimov[4,6,8], A. Lagutchev[2], A. N. Smolyaninov[3], V. V. Klimov[3,8], J. Irudayaraj[5], A. V. Kildishev[1,2], A. Boltasseva[1,2] and V. M. Shalaev[1,2,†]

[1]*School of Electrical and Computer Engineering, Purdue University, West Lafayette, IN 47907, USA*

[2]*Birck Nanotechnology Center, Purdue University, West Lafayette, IN 47907, USA*

[3]*Photonic Nano-Meta Technologies, ul. Lugovaya 4, Skolkovo Innovation Center, Moscow, 143026, Russia*

[4]*Moscow Institute of Physics and Technology, Institutskiy per. 9, Dolgoprudny, Moscow Region, 141700, Russia*

[5]*Agricultural and Biological Engineering, Purdue University, West Lafayette, IN 47907, USA*

[6]*Russian Quantum Center, ul. Novaya 100, BC "Ural", Skolkovo Innovation Center, Moscow Region, 143025, Russia*

[7]*School of Engineering and Physical Sciences, Heriot-Watt University, Edinburgh, Scotland EH14 4AS, United Kingdom*

[8]*Lebedev Physical Institute RAS, Leninskij pr. 53, Moscow, 119991, Russia*

[*] These authors contributed equally to this work.
[†] Electronic mail: shalaev@purdue.edu

S1. Retrieval of dielectric functions

The multilayer metamaterial was characterized by a variable angle spectroscopic ellipsometer (J. A. Woollam Co.; W-VASE). The dielectric functions of the constituent materials (TiN and $Al_{0.7}Sc_{0.3}N$) as well as substrate (MgO) were retrieved from values Ψ and Δ measured in the wavelength range 300 – 2000 nm at angles of incidence 50º and 70º. The Drude-Lorentz model used for fitting is the following:

$$\varepsilon(\hbar\omega) = \varepsilon_1 + i\varepsilon_2 = \varepsilon_\infty + \sum_k \frac{A_k}{E_k^2 - (\hbar\omega)^2 - iB_k\hbar\omega} \quad \text{S(1)}$$

where $\hbar$ is the reduced Plank's constant, A_k is the amplitude, E_k is the center energy and B_k is the broadening of each oscillator [1].

Table S1. Experiment-fitted parameters of the Drude-Lorentz model for (Al,Sc)N and TiN films.

	TiN	(Al,Sc)N
ε_∞	4	4
A_1 $(eV)^2$	52.536	0
B_1 (eV)	0.29197	0
A_2 $(eV)^2$	130.93	11.162
B_2 (eV)	4.9807	0.63261
E_2 (eV)	5.9784	3.6857

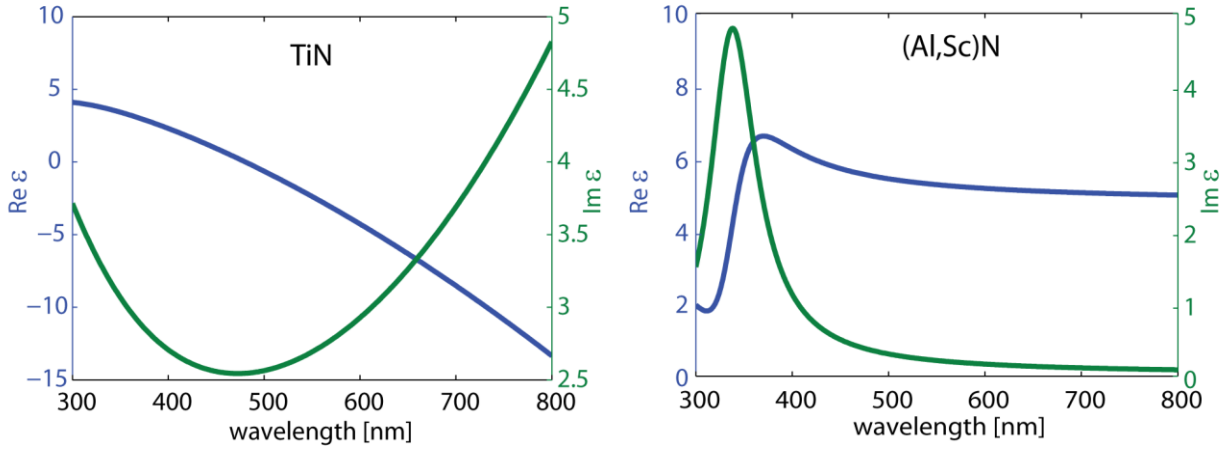

Fig. S1. The dielectric functions of TiN and (Al,Sc)N: real and imaginary parts are shown with blue and green lines, respectively.

S2. Transmittance, reflectance, and absorbance of the HMM sample

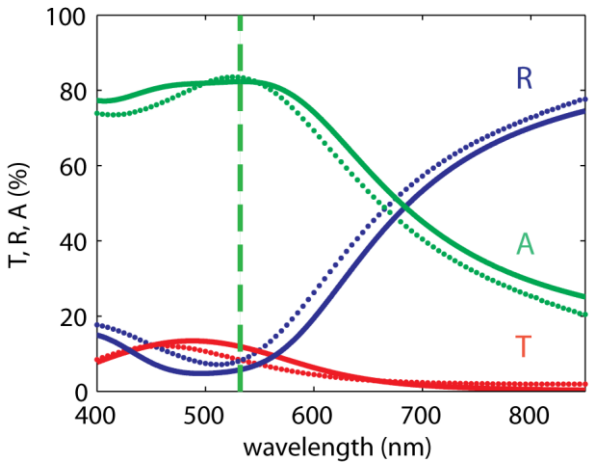

Fig. S2. Transmittance (T), reflectance (R), and absorbance (A) of the TiN HMMs calculated using direct T-matrix method (solid line) **[2]** and measured by spectrophotometry (dotted line); angle of incidence for T – 0°, for R – 8°; A = 1 – T – R.

S3. Semi-analytical calculations of Purcell effect and normalized collected emission power

A single emitter is modeled as an oscillating electric dipole with dipole moment **p** and angular frequency ω. The dipole rate of energy dissipation in an inhomogeneous environment is given by [3]

$$P = \frac{\omega}{2}\mathrm{Im}\left[\mathbf{p}^{*}\cdot\ \mathbf{E}_0(\mathbf{r_0}) + \mathbf{E}_s(\mathbf{r_0})\ \right] \qquad \text{S(2)}$$

where $\mathbf{E}_0(\mathbf{r}_0)$ and $\mathbf{E}_s(\mathbf{r}_0)$ are the primary dipole field and the scattered field at the dipole position $\mathbf{r}_0$, respectively. The electric fields were calculated using the dyadic Green's function formalism [3]. Utilizing angular spectrum representation of the Green's functions allowed us to analyze the contribution of each spatial frequency mode (k-mode).

For a single dipole emitter with in-plane ($\parallel$) or perpendicular ($\perp$) orientation placed at a distance h above a multilayer planar structure, the corresponding Purcell factors F_P can be calculated using the following formulas [3]

$$F_P^{\perp} = 1 + \frac{3}{2}\frac{1}{\varepsilon_{\mathrm{sup}}^{3/2}}\int_0^{\infty}\mathrm{Re}\left\{\frac{s^3}{s_{\perp,\mathrm{sup}}(s)}\tilde{r}^{\mathrm{p}}(s)e^{2ik_0 s_{\perp,\mathrm{sup}}(s)h}\right\}ds\,, \qquad \text{S(3)}$$

$$F_P^{\parallel} = 1 + \frac{3}{4}\frac{1}{\varepsilon_{\mathrm{sup}}^{1/2}}\int_0^{\infty}\mathrm{Re}\left\{\frac{s}{s_{\perp,\mathrm{sup}}(s)}\left[\tilde{r}^{\mathrm{s}}(s) - \frac{s_{\perp,\mathrm{sup}}^2(s)}{\varepsilon_{\mathrm{sup}}}\tilde{r}^{p}(s)\right]e^{2ik_0 s_{\perp,\mathrm{sup}}(s)h}\right\}ds\,, \qquad \text{S(4)}$$

The value of F_P for the statistically averaged (ave) dipole orientation is given by

$$F_P^{ave} = \frac{2}{3}F_P^{\parallel} + \frac{1}{3}F_P^{\perp}\,. \qquad \text{S(5)}$$

Normalized collected emission powers f_{rad} for the same dipole orientations are shown below

$$f_{rad}^{\perp} = \frac{3}{4}\int_{0}^{\theta_{\max}} \sin^3\theta \left| e^{-i\varepsilon_{\sup}^{1/2}k_0 h\cos\theta} + \tilde{r}^{\mathrm{p}}(\theta) e^{i\varepsilon_{\sup}^{1/2}k_0 h\cos\theta} \right|^2 d\theta, \qquad \text{S(6)}$$

$$f_{rad}^{\parallel} = \frac{3}{8}\int_{0}^{\theta_{\max}} \cos^2\theta \left| e^{-i\varepsilon_{\sup}^{1/2}k_0 h\cos\theta} - \tilde{r}^{\mathrm{p}}(\theta) e^{i\varepsilon_{\sup}^{1/2}k_0 h\cos\theta} \right|^2 + \left| e^{-i\varepsilon_{\sup}^{1/2}k_0 h\cos\theta} + \tilde{r}^{\mathrm{s}}(\theta) e^{i\varepsilon_{\sup}^{1/2}k_0 h\cos\theta} \right|^2 \sin\theta d\theta, \qquad \text{S(7)}$$

$$f_{rad}^{ave} = \frac{2}{3} f_{rad}^{\parallel} + \frac{1}{3} f_{rad}^{\perp}. \qquad \text{S(8)}$$

In equations S(3) - S(8), $s = k_{\parallel}/k_0$, $s_{\perp,\sup}(s) = k_{\perp,\sup}(s)/k_0 = \left(\varepsilon_{\sup} - s^2\right)^{1/2}$, $k_0 = \omega/c$, θ is a polar angle measured from the $\perp$ direction, the collection angle $\theta_{\max}$ = 79.6º. The integrals are numerically evaluated by using an adaptive Gauss–Kronrod quadrature method [4]. In the formulas, we assume that the intrinsic quantum yield of NV centers is close to unity.

S4. Calculation of generalized reflection and transmission coefficients of a planar multilayer slab

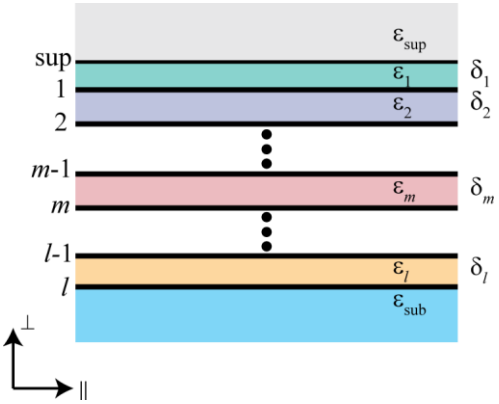

Fig. S3. Schematic of an arbitrary planar lamellar slab consisting of *l* layers.

We use a recursive invariant imbedding [5] to compute generalized reflection coefficients $\tilde{r}^{(\mathrm{p,s})}$ that incorporate the reflection from the *m*-th interface (interface between *m*-th and *m*+1-th layer) and all the subsequent reflections from the interfaces positioned below. The schematic of the structure is shown in Fig. S3. Each layer is characterized by relative permittivity ε_m and thickness δ_m. Above and below the multilayer slab, there are half-spaces of superstrate (ε_{sup}) and substrate (ε_{sub}), respectively. The iterative formula to calculate $\tilde{r}^{(\mathrm{p,s})}(s)$ is the following

$$\tilde{r}_m^{(\mathrm{p,s})}(s) = \frac{r_m^{(\mathrm{p,s})}(s) + \tilde{r}_{m+1}^{(\mathrm{p,s})}(s) e^{i2k_0 s_{\perp,m}(s)\delta_m}}{1 + r_m^{(\mathrm{p,s})}(s)\tilde{r}_{m+1}^{(\mathrm{p,s})}(s) e^{i2k_0 s_{\perp,m}(s)\delta_m}}, \quad m \in \overline{\sup, 1, l} \ , \qquad \text{S(9)}$$

where $s_{\perp,m} = k_{\perp,m}/k_0 = \left(\varepsilon_m - s^2\right)^{1/2}$, where $r_m^{(\mathrm{p,s})}$ are the conventional single-interface Fresnel coefficients

$$r_m^{\mathrm{p}}(s) = \frac{\varepsilon_m s_{\perp,m-1}(s) - \varepsilon_{m-1} s_{\perp,m}(s)}{\varepsilon_m s_{\perp,m-1}(s) + \varepsilon_{m-1} s_{\perp,m}(s)},\ r_m^{\mathrm{s}}(s) = \frac{s_{\perp,m-1}(s) - s_{\perp,m}(s)}{s_{\perp,m-1}(s) + s_{\perp,m}(s)}. \qquad \text{S(10)}$$

The iteration starts from the substrate ($\tilde{r}_{l+1}^{(\mathrm{p,s})}(s) = 0$), then we come up with the seeding iteration ($\tilde{r}_l^{(\mathrm{p,s})}(s) = r_l^{(\mathrm{p,s})}(s)$) and continue with the next step:

$$\tilde{r}_{l-1}^{(\mathrm{p,s})}(s) = \frac{r_{l-1}^{(\mathrm{p,s})}(s) + r_l^{(\mathrm{p,s})}(s) e^{i2k_0 s_{\perp,l-1}(s)\delta_{l-1}}}{1 + r_{l-1}^{(\mathrm{p,s})}(s) r_l^{(\mathrm{p,s})}(s) e^{i2k_0 s_{\perp,l-1}(s)\delta_{l-1}}}. \qquad \text{S(11)}$$

It should be noted that S(11) can be turned into the familiar Drude formula for the reflection coefficient for a single layer of thickness δ [6]:

$$r^{(\mathrm{p,s})}(s) = \frac{r_{1,2}^{(\mathrm{p,s})}(s) + r_{2,3}^{(\mathrm{p,s})}(s) e^{i2k_0 s_\perp(s)\delta}}{1 + r_{1,2}^{(\mathrm{p,s})}(s) r_{2,3}^{(\mathrm{p,s})}(s) e^{i2k_0 s_\perp(s)\delta}}. \qquad \text{S(12)}$$

In the formulas S(6) and S(7), $\tilde{r}^{\mathrm{p}}$ and $\tilde{r}^{\mathrm{s}}$ are expressed as functions of a polar angle θ instead of normalized in-plane wavevector s. The relation between s and θ for the modes propagating in the superstrate medium is $s(\theta) = \varepsilon_{\mathrm{sup}}^{1/2} \sin(\theta)$.

S5. Dependence of emission characteristics on dipole moment orientation and the distance between an emitter and HMM surface

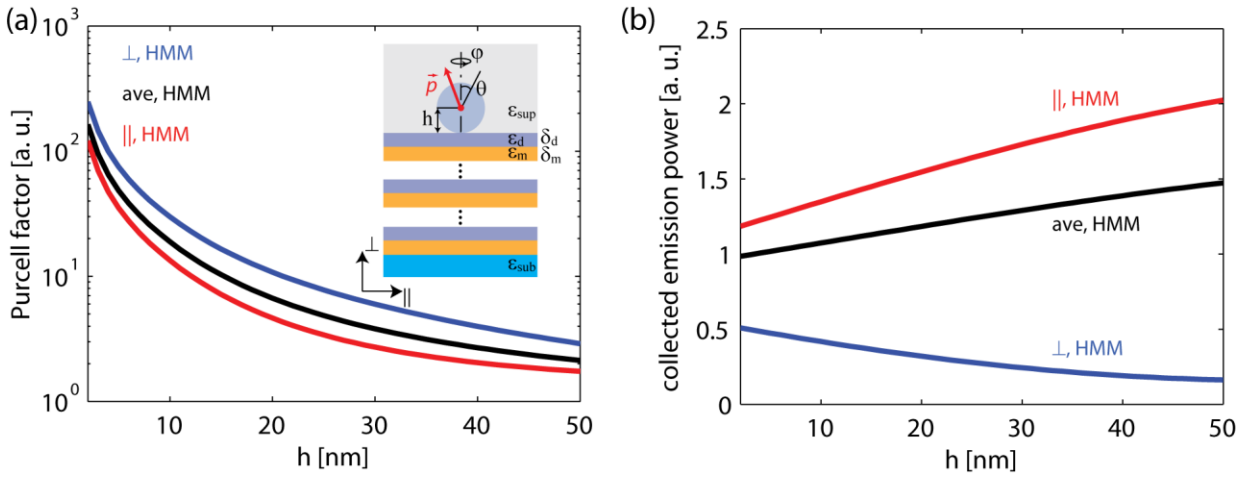

Fig. S4. Dependence of the Purcell factor F_P and the collected emission power f_{rad} on a dipole position h above the HMM surface. Values of F_P and f_{rad} are obtained by averaging the characteristics (shown in Fig. 3 in the main text) over the wavelength range 600-800 nm.

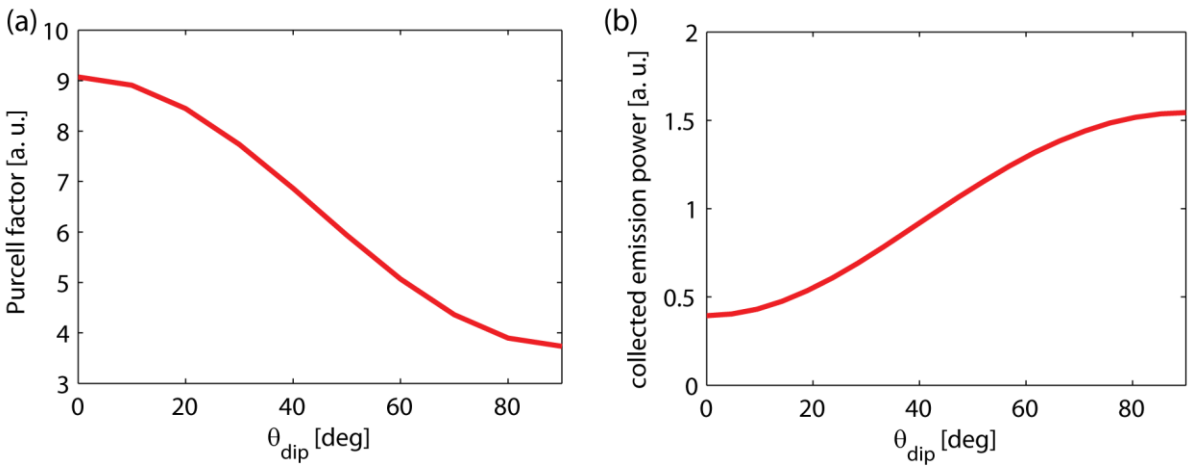

Fig. S5. Dependence of the Purcell factor and the collected emission power on orientation of the emitter's dipole moment. θ_{dip} is a polar angle of the dipole orientation measured from the ⊥ direction.

S6. Influence of neighboring nanodiamonds and structural surface defects of HMM on collected emission power

We have studied the influence of surface superlattice defects and nanodiamonds (NDs) lacking NV centers on collected emission power. Examples of the defects and agglomerated NDs are shown in Fig. 6(a). To qualitatively estimate the influence of these scattering objects, we have performed finite-element method (FEM) analysis using a commercial numerical simulation tool (COMSOL Multiphysics). The schematic of the simulated structure is shown in Fig. 6(b). The HMM is considered as effective anisotropic medium, where scatterers are modelled as either diamond or TiN spheres of 50 nm in diameter. The emitter is emulated by an electric point dipole embedded into 50-nm-diameter diamond sphere. The superstrate and substrate are respectively the immersion oil and MgO. The distance between the emitter and the scatter was taken to be 10 nm, 69 nm, and 343 nm. The emission wavelength was fixed to 685 nm.

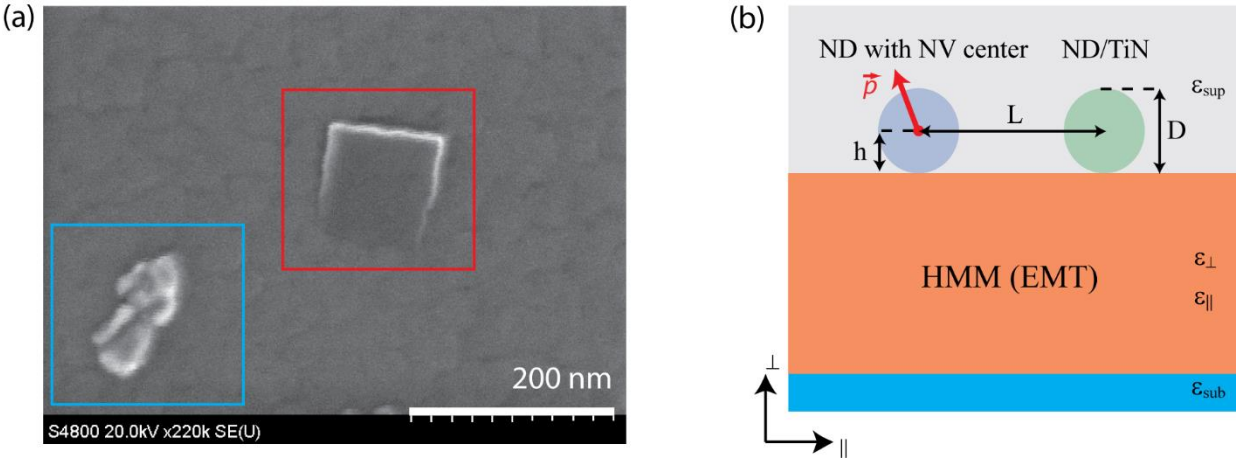

Fig. S6. (a) SEM scan showing a superlattice defect (inside red frame) and agglomerated NDs (inside blue frame). (b) Schematic of the simulated structure.

Results of the FEM simulations are summarized in Table S2. All values of the collected emission powers are normalized by the corresponding powers emitted by the dipole source located on top of the glass coverslip. The noticeable influence is observed at small separation distances (less than 50 nm). For a statistically averaged dipole orientation, an adjacent (at a distance ~10 nm) ND or structural surface defect can increase the collected emission power by 30% or 200%, respectively. For an in-plane oriented emitter, the increase in emitted power from a nearby surface defect could be up to 220%, giving an overall emission enhancement factor of 4. The comparison of the results obtained by using a semi-analytical approach and FEM analysis is shown in Fig. .

Table S2. Influence of NDs lacking NV centers and structural surface defects (TiN particles) on normalized collected emission power.

		on HMM with ND			on HMM with TiN particle		
	on HMM	10 nm	69 nm	343 nm	10 nm	69 nm	343 nm
in-plane (∥)	1.8	2.3	1.8	1.8	3.9	1.9	1.8
perpendicular (⊥)	0.6	0.6	0.6	0.6	0.2	0.4	0.6
averaged (ave)	1.5	1.9	1.5	1.5	3.0	1.5	1.5

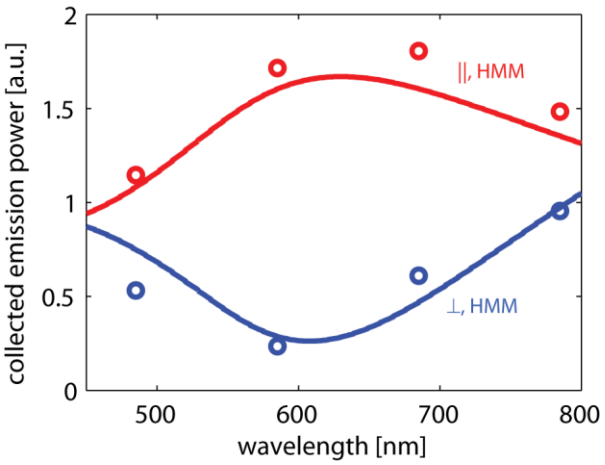

Fig. S7. Agreement between semi-analytical (solid line) and FEM calculations (circles). The calculations are performed for the HMM without any scatterers. Blue and red curves correspond to the dipole orientations perpendicular (⊥) and parallel (||) to the HMM interface, respectively.

References

[1] Guide to Using WVASE 32: Spectroscopic Ellipsometry Data Acquisition and Analysis Software, J. A. Woollam Company, Incorporated, 2008.

[2] P. Yeh, Optical waves in layered media (Wiley, New York, 1988).

[3] L. Novotny and B. Hecht, Principles of Nano-Optics (Cambridge University Press, Cambridge, England, 2006).

[4] L. F. Shampine, J. Comput. Appl. Math., **211**, **2**, 131-140, (2008).

[5] W. C. Chew and S. Y. Chen, Antennas Wirel. Propag. Lett., **2**, **1**, 254-258 (2003).

[6] P. Drude, Ann. Phys., **272**, 865-897 (1889).